

Supplemental Material for

Frustration and Atomic Ordering in a Monolayer Semiconductor Alloy

Amin Azizi^{1,2}, Mehmet Dogan^{1,3}, Jeffrey D. Cain^{1,2,3}, Rahmatollah Eskandari¹, Xuanze Yu⁴, Emily C. Glazer¹, Marvin L Cohen^{1,3}, Alex Zettl^{*,1,2,3}

1. *Department of Physics, University of California at Berkeley, Berkeley, CA, 94720, USA*
2. *Kavli Energy NanoScience Institute at the University of California, Berkeley, Berkeley, CA, 94720, USA*
3. *Materials Sciences Division, Lawrence Berkeley National Laboratory, Berkeley, CA, 94720, USA*
4. *Department of Materials Science and Engineering, University of California at Berkeley, Berkeley, CA, 94720, USA*

* Corresponding Author. E-mail: azettl@berkeley.edu , Phone: +1 (510) 642-4939 Fax: +1 (510) 642-2685

Materials and Methods

Growth of $\text{Re}_{0.5}\text{Nb}_{0.5}\text{S}_2$ Crystals. Bulk single crystals of $\text{Re}_{0.5}\text{Nb}_{0.5}\text{S}_2$ are synthesized using chemical vapor transport with a halide transport agent. Elemental powders of rhenium (Aldrich, 99.995%), niobium (Alfa Aesar, 99.8%), and sulfur (Alfa Aesar, 99.5%) are mixed (approximately 1 gram total precursor amount) and sealed into a quartz tube ($L=20$ cm, $d=1$ cm) with 80 mg of iodine (Alfa Aesar, 99.5%) under high vacuum (10^{-6} Torr). The crystals are grown in a mild temperature gradient of 960-930°C for 21 days, before cooling naturally. The result is many small (~1mm), silver single crystals with platelet like morphology, that can be readily exfoliated with scotch tape (see Fig. S1).

Scanning Transmission Electron Microscopy (STEM) and Energy Dispersive X-ray Spectroscopy (EDS) characterization.

Annular dark field scanning transmission electron microscopy (ADF-STEM), as a widely used technique to probe the atomic structure of transition metal dichalcogenides (TMDs) [26–29], is performed to uncover atomic ordering in the $\text{Re}_{0.5}\text{Nb}_{0.5}\text{S}_2$ alloy. An aberration-corrected FEI Titan3 (60–300) equipped with a SuperX energy dispersive X-ray spectrometry (EDS) system at 80 kV is used for the imaging and spectroscopy. We use a camera length of 115 mm, a

convergence angle of 30 mrad, an inner collection angle of 42 mrad, and a beam current of 50 pA for image acquisition. EDS elemental mapping (Fig. S2) is performed in the STEM mode at 80 kV with a 7min acquisition time.

Infrared Micro-Spectroscopy Measurements. Infrared micro-spectroscopy measurements are carried out at the Advanced Light Source (Beamline 1.4) at Lawrence Berkeley National Laboratory. Measurements are collected on Nicolet iS50 FTIR in transmission mode. Few- and monolayer samples are first exfoliated onto PDMS stamps, and optical contrast is used to determine layer number (see Fig. S1), they are then deposited onto transparent quartz substrates for infrared measurements.

Theoretical methods. We compute total energies using density functional theory (DFT) in the Perdew-Burke-Ernzerhof Generalized Gradient Approximation (PBE GGA) [30] with norm-conserving pseudopotentials. We use the QUANTUM ESPRESSO software package to perform the calculations with a plane-wave basis with an energy cutoff of 80 Ry [31]. A 12×12 Monkhorst-Pack k-point mesh is used to sample the 1×1 unit cells, and a 0.01 Ry Marzari-Vanderbilt smearing is employed [32]. For thin film simulations, periodic copies of the slab are separated by 12 Å of vacuum in the z-direction. Cell parameter and atomic relaxations are done using the BFGS algorithm. All atomic positions are relaxed until the forces on the atoms are less than 10^{-4} Ry/Bohr in magnitude along all Cartesian directions. We include the van der Waals interactions using the semiempirical DFT-D2 method [33,34].

Supplementary Text

Total energies of $\text{Re}_x\text{Nb}_{(1-x)}\text{S}_2$ alloys with varying composition. We compute the total energies of $\text{Re}_x\text{Nb}_{(1-x)}\text{S}_2$ monolayers in the 1H, 1T and 1T' configurations, where $x = 0, 1/16, \dots, 15/16, 1$. For each composition, we estimate the lowest energy configuration by separating the metal ions of the same kind as much as possible in 4×4 cells. For each simulation, after setting up the initial atomic positions using the 1H and 1T phases of NbS_2 and the 1T' phase of ReS_2 , we allow the atoms to relax in all directions. As a result, the distortions in the 1T' phase of the compositions close to NbS_2 (small x) diminish, while the 1T phase configurations for the compositions close to ReS_2 (large x) become distorted. Thus, we find that the 1T and the 1T' phases do not coexist for a

given composition, and the distortion from 1T gradually increases as x increases for all the $\text{Re}_x\text{Nb}_{(1-x)}\text{S}_2$ monolayers. In addition, we observe that for $x > 0.75$, the 1H phase also distorts due to the relaxation of some of the Re atoms away from their high symmetry positions in the plane of the monolayer. For pure ReS_2 , where the distortions are largest, this 4×4 1H phase lies at -0.33 eV/ MS_2 with respect to the high-symmetry 1×1 1H phase. However, because we impose $z\rightarrow -z$ mirror symmetry in the initial setup of the 1H phase configurations, the S atoms in the symmetric positions are prevented from relaxing into different in-plane positions. Therefore, it is possible that for high x , the 1H phase is dynamically unstable and would relax into the $1\text{T}'$ phase if allowed by symmetry. The in-plane distortions in the 1H structures of $x > 0.75$ are demonstrated in Fig. S3. In the figure, it is observed that the variations in the Re-S bond lengths and the angles in the hexagonal grid increases as x increases. For $x \leq 0.75$, the homogeneously distributed Nb atoms stabilize the threefold 1H symmetry. In Fig. S4, we demonstrate the fact that the threefold 1H symmetry is approximately preserved for $x = 0.5$ configurations. After relaxing 24 configurations in the 6×6 cell (12 from the experimental Re/Nb distributions and 12 from random Re/Nb distributions), we have found that the atoms do not displace greatly from their ideal 1H positions (4 such configurations are shown in Fig. S4 as examples). In fact, all the in-plane displacements are less than 9 pm, and the average displacement is 4 pm with a standard deviation of 2 pm. Among the 6×6 configurations, the energy reduction by allowing these distortions is 38 meV/ MS_2 with a standard deviation of 2 meV/ MS_2 . Moreover, if we only consider the positions of the Nb and Re atoms and their deviations from the ideal triangular lattice, we find that the average displacement is 1 pm with a standard deviation of 1 pm, and the maximum displacement is 3 pm. This shows that the 50%-50% alloy is almost perfectly approximated by the 1H phase with very small displacements (mostly in the positions of the sulfur atoms).

The resulting total energies for the varying compositions are presented in Fig. 1d, where the energy of the 4×4 1H phase is taken as reference for each x . We see that a compositional phase transition from 1H to $1\text{T}'$ occurs at $x = 0.68$. For pure NbS_2 , the 1T phase is found to be 0.08 eV/ MS_2 higher in energy than the 1H phase. For pure ReS_2 , the $1\text{T}'$ phase is 0.66 (0.99) eV/ MS_2 more stable than the 4×4 1H (1×1 1H) phase.

Formation energy of $\text{Re}_x\text{Nb}_{(1-x)}\text{S}_2$ alloys with respect to the two parent components. After determining the ground state configuration for each composition, we compute the formation energy of that configuration, defined as the total energy of that configuration with respect to the two parent TMD components:

$$E_f(x) = E(\text{Nb}_{(1-x)}\text{Re}_x\text{S}_2) - (1-x)E(\text{NbS}_2) - xE(\text{ReS}_2)$$

We show the resulting formation energies in Fig. 1e. We find that the alloys are stable up to $x = 0.63$ with the $x = 0.50$ alloy being the most stable with respect to its components. Our result of $E_f(0.5) = -0.21$ eV/ MS_2 agrees well with the previous computational result of -0.24 eV/ MS_2 [15].

Quantification of different nearest-neighbor number (DNN), spatial correlation functions, and the stripe length. We analyze 20 unit-cell by 20 unit-cell supercells of STEM images from various regions of the $\text{Re}_{0.5}\text{Nb}_{0.5}\text{S}_2$ sample. Such an image is shown in Fig. 2b. We quantify the average DNN ($\overline{\text{DNN}}$) and find a preference for metal atoms to be adjacent to the atomic species of the other kind. This is analogous to antiferromagnetic Ising spins, which leads to geometrical frustration in a triangular lattice. In such a system, there is an energy cost for having two parallel spins as nearest neighbors, yet it is not possible to have all nearest-neighbor pairs be anti-parallel as in a square lattice. In short, this lattice can be thought of as consisting of triangles in which each nearest-neighbor interaction is part of only one triangle (Fig. S5). For any such triangle, there has to be at least one pair of parallel spins. If all the triangles have only one pair of parallel spins, the energy is minimized. Such a configuration is possible if up and down spins are arranged in alternating rows. Therefore, the largest possible value of $\overline{\text{DNN}}$ is 4.

Up and down spins correspond to Nb and Re atoms in our system, and the triangular lattice is the transition metal sub-lattice. If the distribution of atoms in the alloy is solely driven by a nearest-neighbor interaction, the structure shown in Fig. 1c would then correspond to a ground state. However, in the limit where the system size goes to infinity, there are infinitely many ground state configurations for the frustrated triangular lattice of Ising antiferromagnets. In fact, this system has no critical temperature at which an order-disorder transition happens; instead its entropy

gradually increases from $S(T = 0) = 0.323R$ to $S(T \rightarrow \infty) = 0.693R$, where R is the molar gas constant.

The Nb/Re atoms form a triangular sub-lattice with three principle directions. We compute the spatial correlation functions in these directions, defined as:

$$C_{\vec{a}}(\Delta x) = \langle \sigma(\vec{x})\sigma(\vec{x} + \Delta x\vec{a}) \rangle_{\vec{x}} - \langle \sigma(\vec{x}) \rangle_{\vec{x}} \langle \sigma(\vec{x} + \Delta x\vec{a}) \rangle_{\vec{x}},$$

where $\sigma(\vec{x})$ identifies the metal (0 for Nb, 1 for Re) at the lattice site at \vec{x} , $\langle \rangle_{\vec{x}}$ operation stands for averaging over all \vec{x} , and \vec{a} stands for the three principle directions (0° , 60° and 120° from the lattice vector \vec{a}). We assume periodic boundary conditions in calculating the correlation functions. The results are presented in Fig. 2e. We observe that $C_{\vec{a}}(0) = 0.25$ for all directions, which is expected since $\sigma(\vec{x}) = 0$ for half of the sites, and 1 for the other half. $C_{\vec{a}}(1)$ is between -0.06 and -0.08 for all directions, and $C_{\vec{a}}(\Delta x)$ fluctuates around zero for $\Delta x > 1$.

In addition, the lengths of homoatomic stripes along the three zigzag directions (extracted from the ADF-STEM image in Fig. 2b) are calculated by counting the number of consecutive Nb or Re atoms along a given direction until the atom of the other kind is encountered. The histograms of the stripe length along the three zigzag directions are presented in Figure 2f.

Nearest-neighbor-based model of the distribution of atomic species. To build a nearest-neighbor-based model to explain the distribution of atomic species, we run 60 DFT simulations in cells varying from 4×3 to 6×6 . To include configurations with low $\overline{\text{DNN}}$ values, we use 10×1 , 12×1 , 14×1 and 16×1 cells. The 6×6 structures in the dataset consist of 12 experimental and 12 random configurations. For each simulation, we compute the $\overline{\text{DNN}}$ and relax all the atomic coordinates to find the total energy. We find that introducing the second nearest neighbors to the model does not improve the fit. We note that $\overline{\text{DNN}}$ alone does not determine the total energy, and for a given $\overline{\text{DNN}}$, energy can change up to 0.04 eV according to our calculated values. However, this spread, which is less than 0.02 eV for most configurations, is an order of magnitude smaller than the effect of changing the $\overline{\text{DNN}}$ (according to our model, the energy cost of decreasing $\overline{\text{DNN}}$ by 1 is 0.15 eV).

Another helpful way to characterize the heteroatomic nearest neighbor tendency in this system is to examine the triplets of atomic species [20]. A triplet is defined as three lattice sites, where, among the three pairs of these sites, at least two are nearest neighbor pairs. Three types of triplets are possible: linear triplet (LT), bent triplet (BT) and triangular triplet (TT). In an LT, the three atoms are on a straight line; in a BT, they make a 120° angle; in a TT, they make up an equilateral triangle. If all three sites of a triplet are occupied by an Re (Nb) atom, the triplet is called an Re (Nb) triplet. Following Ref. [20] we expect the probability for an atom to be in an Re or Nb LT/BT to be equal to

$$p(\text{LT}) = p(\text{BT}) = \frac{1}{2} \left(1 - \frac{\overline{\text{DNN}}}{6} \right)^2,$$

where $\overline{\text{DNN}}$ denotes the average DNN over the whole system, whereas, the probability for an atom to be in an Re or Nb TT is

$$p(\text{TT}) = \left(1 - \frac{\overline{\text{DNN}}}{6} \right)^3.$$

For a random system with $\overline{\text{DNN}} = 3$, all of these probabilities are equal to $\frac{1}{8}$. For a system with $\overline{\text{DNN}} = 4$, however, we expect $p(\text{LT}) = p(\text{BT}) = \frac{1}{18}$ and $p(\text{TT}) = \frac{1}{27}$. In Table S1, we list the values for these probabilities as computed for the configurations in Figure 3c-e.

Thermodynamics of species distribution at finite temperature. To explore the thermodynamics of species distribution at finite temperature in our alloys, we solve our nearest neighbor model using Monte Carlo simulations in the Metropolis algorithm [21]. For each temperature, we start with a 20 unit cell by 20 unit cell grid where a random half of the sites are assigned 0 (Nb) and the other half 1 (Re). Then, a pair of Nb and Re sites are randomly chosen. The change in energy (ΔE) due to switching the states in this pair of sites is computed, and the switching occurs with probability 1 if $\Delta E < 0$, and with probability $e^{-\Delta E/k_B T}$ if $\Delta E \geq 0$. We monitor the thermalization of the simulation runs using the time correlation (autocorrelation) function [22]. Because this model does not have a critical temperature, the simulation runs easily thermalize, *i.e.* the phase space is well-sampled.

At each temperature, ten simulations are run, and the plotted values reflect the averages and the standard deviations among those runs. The results for the $\overline{\text{DNN}}$ vs. temperature are presented in Fig. 3b. We note that the agreement between our thermodynamic model and the experimentally grown alloys does not necessarily mean that the model provides a full picture of the growth processes. Indeed, switching the atoms between different lattice sites is a complicated chemical process with energy barriers that introduce time scales into the thermalization. These effects are not considered in our model.

Calculations of thickness-dependent bandgap of $\text{Re}_{0.5}\text{Nb}_{0.5}\text{S}_2$. In order to check the dependence of bandgap on the thickness and stacking sequence of the reference $\text{Re}_{0.5}\text{Nb}_{0.5}\text{S}_2$, we construct all possible high-symmetry stacking sequences that can occur in the bilayer systems. After eliminating the seven stackings that are 12-82 meV/ MS_2 higher in energy than the lowest energy stacking, we are left with six stacking sequences that are all within 7.8 meV/ MS_2 of the lowest energy stacking. We list the total energies as well as the bandgap for bilayer and bulk of these stacking sequences in Table S2. For the calculations with more than two layers, we assume that the stacking sequence repeats with a periodicity of 2. We present the atomic structures of the six lowest-energy stackings in Fig. S6, and the band structures of the monolayer and a representative bilayer configuration in Fig. S7.

We should note the reference structure (Fig. 1c) with long-range order is used for calculations of the bandgap for multilayer crystals. Therefore, the excellent agreement between theory and experiment can be attributed to the fact that the underestimation of the gap by DFT (usually in the 30%-70% range) is cancelled by the overestimation of the gap by the long-range ordered of the reference structure (here ~50%). As a separate note, the considerable difference between the bandgap of experimental and random configurations can be attributed to the fact that the Coulomb potential at each transition metal site is mostly determined by its nearest neighbors. In the experimental configurations, $\text{DNN} \geq 2$ for almost all the sites, whereas the DNN for the random configurations can be 0 to 6 (Figs. 3d-e). This larger spread for the random configurations causes the valence and the conduction states to have a larger energy spread, reducing the bandgap.

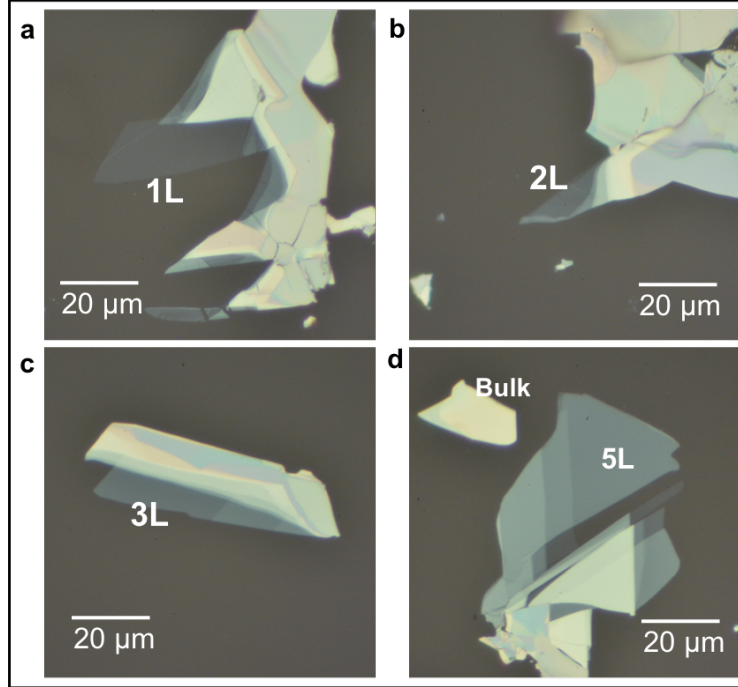


Fig. S1 | Optical images of the Re_{0.5}Nb_{0.5}S₂ crystals with different layer numbers used for optical measurements. a, 1L, b, 2L, c, 3L, and d, 5L and bulk (*i.e.* the thickest exfoliated flake) crystals on PDMS.

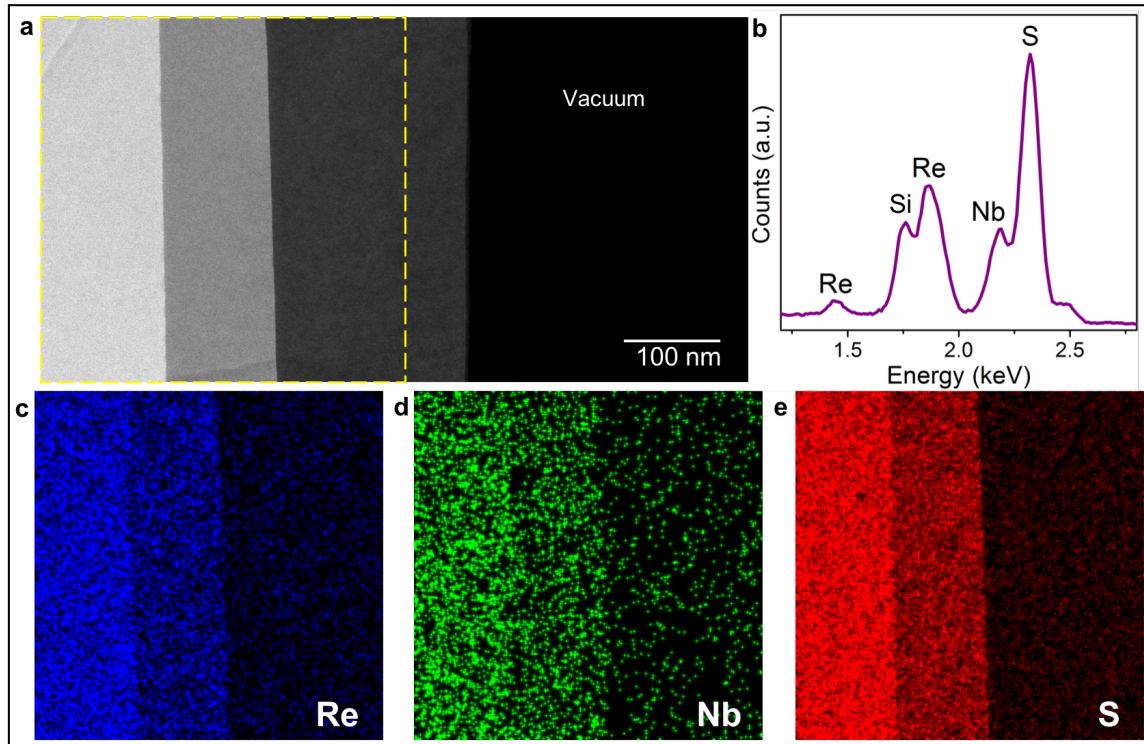


Fig. S2 | Chemical composition analysis of the grown Re_{0.5}Nb_{0.5}S₂ crystals using energy dispersive X-ray spectroscopy (EDS). a, Annular dark-field scanning transmission electron

microscopy (ADF STEM) image of a few-layer $\text{Re}_{0.5}\text{Nb}_{0.5}\text{S}_2$ crystal suspended over a hole of the TEM grid. **b**, EDS spectrum showing peaks of Re, Nb, and S. the Si peak comes from the silicon nitride TEM grid. **c-e**, EDS elemental maps of Re, Nb, and S respectively, from the region marked on the ADF-STEM image in **a**, showing uniform distribution of Re, Nb, and S.

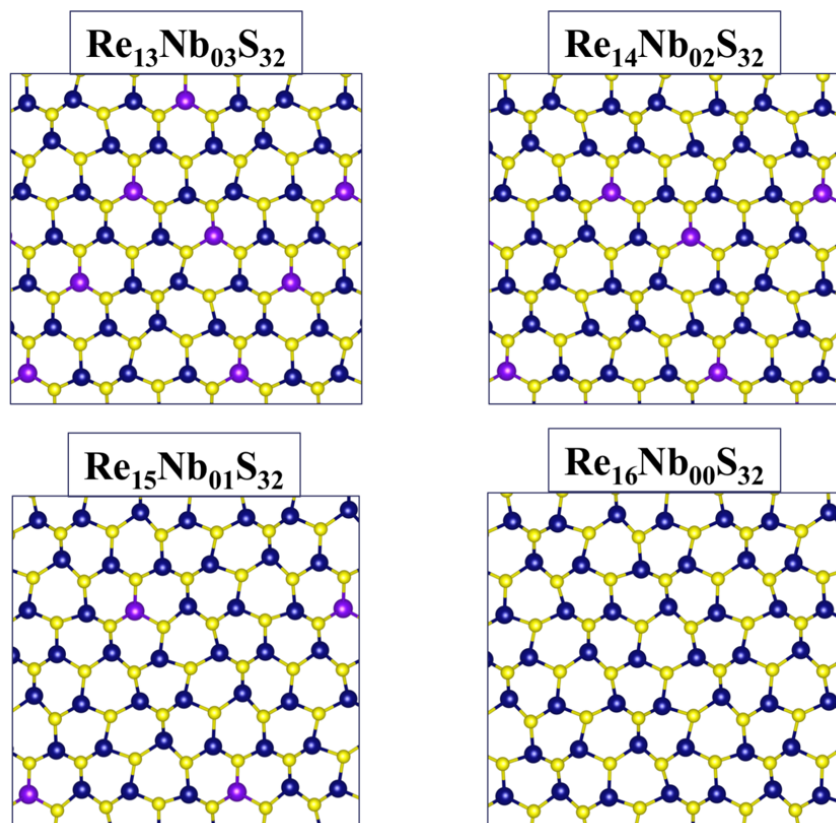


Fig. S3 | Breaking of the in-plane threefold symmetry in the 1H $\text{Re}_x\text{Nb}_{(1-x)}\text{S}_2$ configurations for large x, when the atomic positions are allowed to relax in the 4x4 unit cell (Re: navy, Nb: light violet, S: yellow).

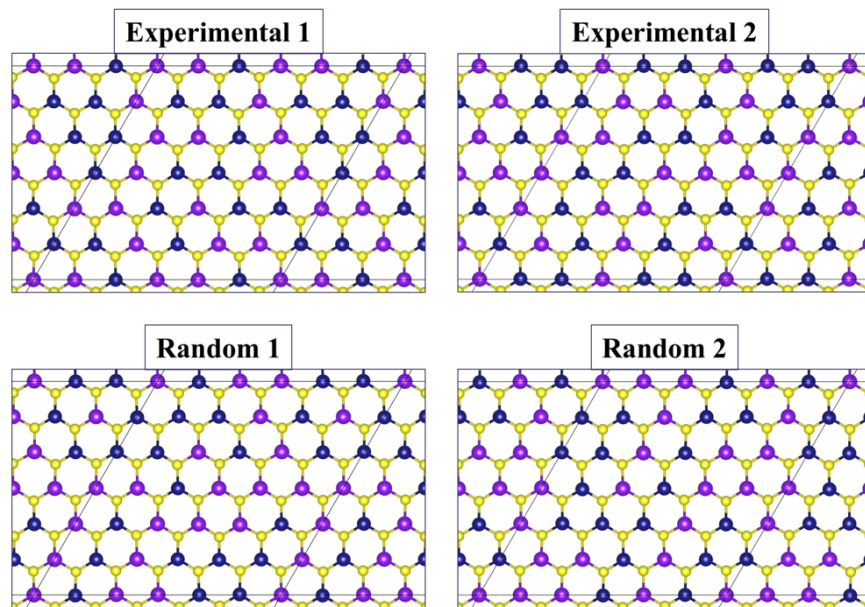


Fig. S4 | Preservation of the in-plane threefold symmetry in the 1H $\text{Re}_{0.5}\text{Nb}_{0.5}\text{S}_2$ configurations, when the atomic positions are allowed to relax in the 6×6 unit cell (Re: navy, Nb: light violet, S: yellow). For the top two, the distribution of the Re and Nb atoms are taken from experimental images; for the bottom two, the Re and Nb atoms are randomly distributed.

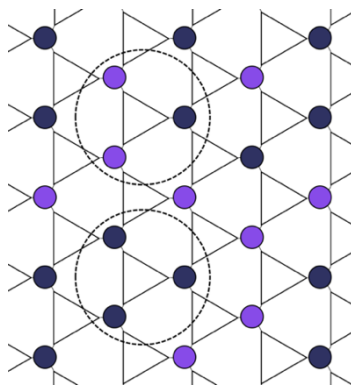


Fig. S5 | Decomposition of the triangular sub-lattice of transition metal atoms into individual triangles. Navy (Re) and violet (Nb) colors can be also seen as spin-up and spin-down states. The triangles correspond to a unique representation of all the nearest-neighbor interaction in the lattice, where each triangle edge corresponds to one and only one nearest-neighbor pair. The total energy of the lattice is thus equal to the sum of the interaction energies of all triangles. For such a configuration, it is not possible to make all three edges of a triangle heterospin. Instead, the most energetically favorable configuration of a triangle is where two of the edges are heterospin, and one is homospin, as seen in the top circled triangle. The only other combination is where all three edges are homospin, as seen in the bottom circled in triangle.

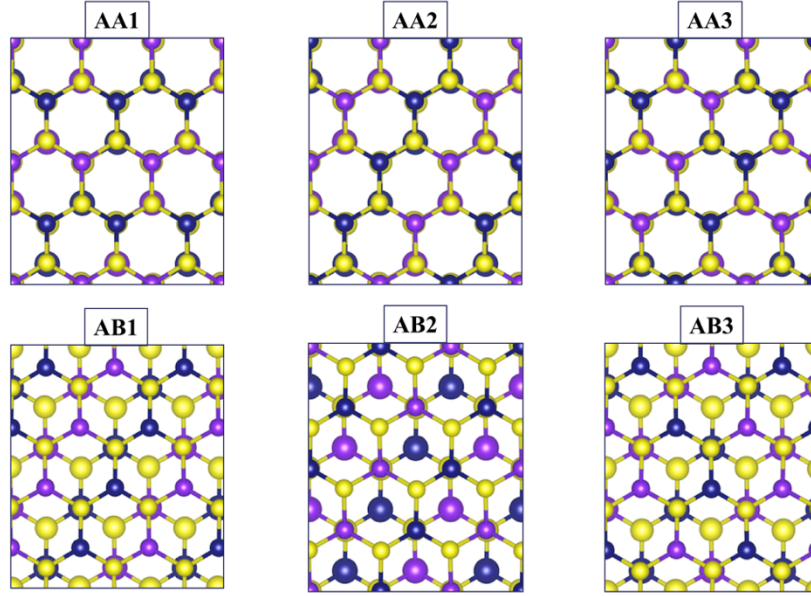


Fig. S6 | Six lowest-energy stackings of the bilayer configurations of the reference $\text{Re}_{0.5}\text{Nb}_{0.5}\text{S}_2$ structure, computed by DFT (Re: navy, Nb: light violet, S: yellow).

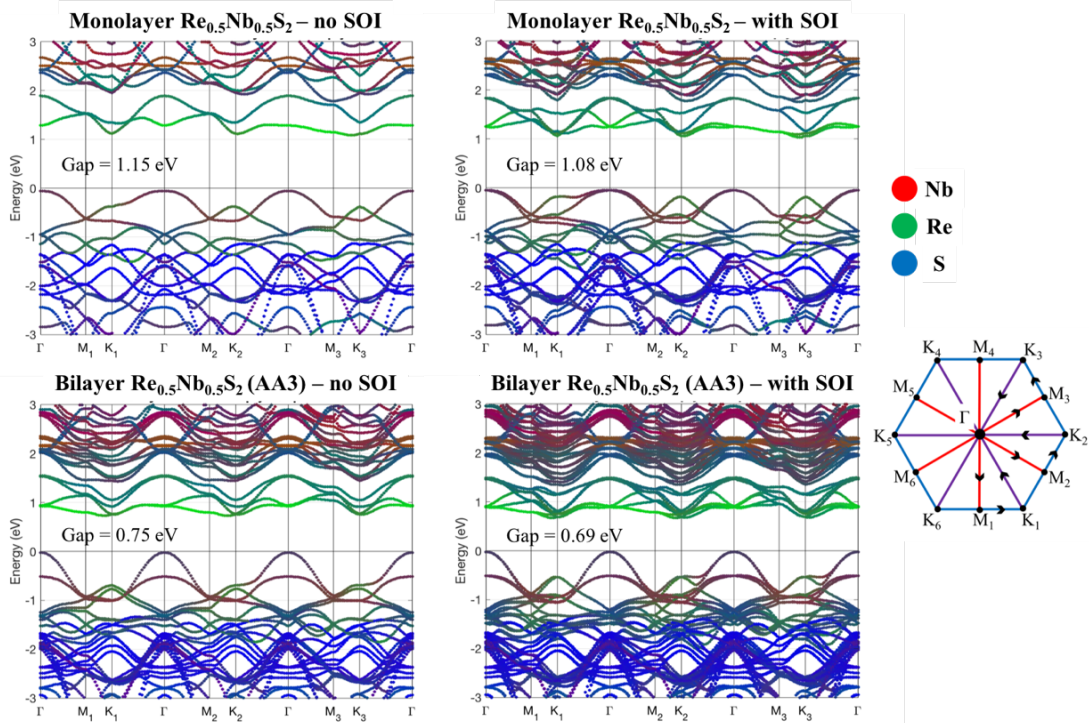


Fig. S7 | Band structures of the monolayer and bilayer (AA3) configurations of the reference $\text{Re}_{0.5}\text{Nb}_{0.5}\text{S}_2$ structure, computed by DFT. Calculations both with and without spin-orbit interaction are shown. For each (k-point, band number) pair, the projections of the eigenfunction onto the atomic orbitals of the three component atoms are computed, and the point is colored based on these projections (Re: green, Nb: red, S: blue). The high-symmetry paths in the first Brillouin zone used in the plots are also shown.

Table S1 | The probability of an atom to be in an Re or Nb triplet, for three triplet types (LT, BT and TT), and for the three configurations presented in Figure 3. The expected values according to the formulas given in the text are also presented in parentheses.

	$p(\text{LT})$	$p(\text{BT})$	$p(\text{TT})$
Theory - Figure 3c	0.066 (0.065)	0.065 (0.065)	0.046 (0.048)
Experiment - Figure 3d	0.065 (0.066)	0.068 (0.066)	0.044 (0.047)
Random - Figure 3e	0.124 (0.125)	0.124 (0.125)	0.126 (0.125)

Table S2 | Bandgap of the six lowest-energy multilayer configurations of the reference $\text{Re}_{0.5}\text{Nb}_{0.5}\text{S}_2$ structure, computed by DFT with spin-orbit interaction included. In the last row, the total energies with respect to the AB2 stacking for the bilayer crystals are shown.

	Band gap (eV) in DFT with spin-orbit interaction					
Thickness	AA1	AA2	AA3	AB1	AB2	AB3
1	1.08	1.08	1.08	1.08	1.08	1.08
2	0.69	0.75	0.66	0.62	0.66	0.65
3	0.58	0.65	0.53	0.50	0.57	0.56
4	0.54	0.62	0.49	0.46	0.53	0.52
Bulk	0.45	0.56	0.38	0.35	0.43	0.41
E (meV)	4.1	0.4	7.8	7.0	0.0	3.6

REFERENCES

- [26] A. Azizi, X. Zou, P. Ercius, Z. Zhang, A. L. Elías, N. Perea-López, G. Stone, M. Terrones, B. I. Yakobson, and N. Alem, Nat. Commun. **5**, 4867 (2014).
- [27] A. M. van der Zande, P. Y. Huang, D. a Chenet, T. C. Berkelbach, Y. You, G.-H. Lee, T. F. Heinz, D. R. Reichman, D. a Muller, and J. C. Hone, Nat. Mater. **12**, 554 (2013).
- [28] A. Azizi, S. Eichfeld, G. Geschwind, K. Zhang, B. Jiang, D. Mukherjee, L. Hossain, A. F. Piasecki, B. Kabius, J. A. Robinson, and N. Alem, ACS Nano **9**, 4882 (2015).
- [29] A. Azizi, Y. Wang, G. Stone, A. L. Elias, Z. Lin, M. Terrones, V. H. Crespi, and N. Alem, Nano Lett. **17**, 2802 (2017).
- [30] J. P. Perdew, K. Burke, and M. Ernzerhof, Phys. Rev. Lett. **77**, 3865 (1996).
- [31] P. Giannozzi, S. Baroni, N. Bonini, M. Calandra, R. Car, C. Cavazzoni, D. Ceresoli, G. L. Chiarotti, M. Cococcioni, I. Dabo, A. Dal Corso, S. de Gironcoli, S. Fabris, G. Fratesi, R.

- Gebauer, U. Gerstmann, C. Gougoussis, A. Kokalj, M. Lazzeri, L. Martin-Samos, N. Marzari, F. Mauri, R. Mazzarello, S. Paolini, A. Pasquarello, L. Paulatto, C. Sbraccia, S. Scandolo, G. Sclauzero, A. P. Seitsonen, A. Smogunov, P. Umari, and R. M. Wentzcovitch, *J. Phys. Condens. Matter* **21**, 395502 (2009).
- [32] N. Marzari, D. Vanderbilt, A. De Vita, and M. C. Payne, *Phys. Rev. Lett.* **82**, 3296 (1999).
- [33] S. Grimme, *J. Comput. Chem.* **27**, 1787 (2006).
- [34] V. Barone, M. Casarin, D. Forrer, M. Pavone, M. Sami, and A. Vittadini, *J. Comput. Chem.* **30**, 934 (2009).